Laser & Photonics Reviews

LASER & PHOTONICS REVIEWS

www.lpr-journal.org

RESEARCH ARTICLE OPEN ACCESS

Tailoring SHG Efficiency via t-Te Nanocrystals in Tellurite Glasses by Femtosecond Laser Micromachining

José Luis Clabel Huamán | Kelly Tasso de Paula | José Dirceu Vollet-Filho | Euclydes Marega Junior | Lino Misoguti | Cleber Renato Mendonça

São Carlos Institute of Physics, University of São Paulo, São Carlos, São Paulo, Brazil

Correspondence: José Luis Clabel Huamán (jclabel@ifsc.usp.br) | Cleber Renato Mendonça (crmendon@ifsc.usp.br)

Received: 6 October 2025 | **Revised:** 28 October 2025 | **Accepted:** 29 October 2025

Keywords: nonlinear properties | perovskite | SHG | tellurite-zinc glass | t-Te nanocrystals

ABSTRACT

In this study, we propose a strategy to enhance and modulate second-harmonic generation (SHG) in tellurite-zinc (TZ) glasses via femtosecond (fs) laser microfabrication, with and without the incorporation of $BaTiO_3$:Er/Yb/Zn nanoparticle (TZ-NP). Fs-laser irradiation at varied fluences induces structural modifications, as revealed by Raman spectroscopy and mapping, including an increase in the $I(TeO_3)/I(TeO_4)$ ratio (~15% in TZ and ~21% in TZ-NP), indicative of network depolymerization, NBO formation, and densification. Trigonal tellurium (t-Te) nanocrystals nucleate and grow under irradiation, exhibiting a chiral, non-centrosymmetric structure, as evidenced by the emergence of A_1 and E_{TO} Raman modes (~120 cm^{-1} and ~140 cm^{-1}), XRD peaks matching the $P3_121$ t-Te phase, and HRTEM showing nanocrystals expanding from ~8 nm to ~16 nm with increasing pulse number. Complementary atomic-resolution imaging and SAED confirm lattice ordering and long-range periodicity along [001], reinforcing the formation of non-centrosymmetric, SHG-active domains. Optical and confocal imaging under 850 nm and 980 nm excitation reveal localized SHG and, in TZ-NP, upconversion luminescence, with SHG intensity peaking at 1.9 J/cm^2 in TZ (850 nm) and reaching 3.3 J/cm^2 (850 nm) and 4.2 J/cm^2 (980 nm) in TZ-NP. Quantitative scaling laws ($I_{2\omega} \propto F^m$) and a figure of merit ($\sqrt{\varepsilon}$) further confirm nanoparticle-induced enhancement of SHG efficiency. These results demonstrate that fs-laser-induced crystallization of t-Te, combined with local field enhancement from perovskite nanoparticles, enables efficient and tunable SHG in tellurite-based glasses, offering new avenues for integrated nonlinear photonic platforms.

1 | Introduction

Nonlinear optical phenomena, particularly second-harmonic generation (SHG), are foundational to photonic applications such as frequency conversion and signal modulation [1, 2]. Among nonlinear glass systems, tellurite-zinc (TZ) glass stands out for its high third-order susceptibility, low phonon energy, and broad infrared transparency [3–5].

However, the intrinsic centrosymmetry of glasses suppresses electric-dipole-allowed second-order responses. To overcome this, techniques such as thermal or electrical poling and in situ crystallization have been employed to locally break inversion symmetry, enabling effective second-order susceptibility (χ^2) and SHG activation in otherwise inactive matrices [1, 6]. Recent developments in femtosecond (fs) laser direct writing have introduced an additional route for spatially selective symmetry breaking [6–8]. Fs-laser irradiation induces structural rearrangements, including $TeO_4 \rightarrow TeO_3$ conversion, formation of non-bridging oxygens (NBOs), densification, and even the nucleation of crystalline phases, enabling confined nonlinear regions in tellurite glasses [9, 10].

Of particular interest is the laser-induced crystallization of trigonal tellurium (t-Te), whose chiral, non-centrosymmetric phases ($P3_121$ or $P3_221$) intrinsically support SHG via electric-dipole

transitions [11–13]. Although previous studies have reported elemental Te formation under fs irradiation, the mechanisms governing t-Te nucleation and its direct correlation with SHG output remain poorly understood [14, 15].

Here, we address this gap by directly linking t-Te nanocrystal formation to symmetry breaking and SHG activation. Compared to other oxide systems, tellurite glasses exhibit enhanced susceptibility to fs-laser-induced crystallization, making them ideal candidates for 3D microstructuring of nonlinear optical components [16–19]. To explore compositional effects, we investigate both pure TZ and incorporating $BaTiO_3$:Er/Yb/Zn nanoparticle (TZ-NP). The nanoparticles enhance local fields, promote upconversion luminescence, and modulate energy deposition through altered electron-phonon interactions.

Advanced Raman mapping of the $I(TeO_3)/I(TeO_4)$ ratio serves as a spectroscopic probe of local depolymerization, while the emergence of sharp vibrational modes near 120 $cm^{-1}$and 140 cm^{-1} provides direct evidence of t-Te crystallization. These structural changes are further correlated with SHG and upconversion signals.

In this work, we demonstrate that fs-laser microfabrication enables controlled SHG enhancement in TZ and TZ-NP glasses through a dual mechanism: network rearrangement and redox-driven crystallization. By combining microfabrication with Raman imaging, XRD, HRTEM, χ^2-type nonlinear optical measurements (SHG), and upconversion luminescence analysis under 850 and 980 nm excitation, we establish a scalable and compositionally tunable platform for integrated photonic applications in frequency conversion, optical modulation, and rare-earth-based light emission.

2 | Results and Discussion

2.1 | Fs-Laser Processing and Surface Morphology

Pure tellurite-zinc (TZ) and tellurite-zinc glasses incorporating $BaTiO_3$:Er/Yb/Zn nanoparticle (TZ-NP) were microfabricated via femtosecond laser irradiation to enhance second-harmonic generation (SHG). X-ray diffraction (XRD) confirmed that both glass systems remain fully amorphous after nanoparticle incorporation, suggesting either nanoscale dispersion or structural disruption of the crystalline phase, as reported previously [20]. Such incorporation strategies are commonly employed to modulate local fields and enhance nonlinear optical responses.

Due to their wide optical transparency (400–1000 nm) and low linear absorption coefficients (0.06 cm^{-1} between 800 and 1100 nm), both TZ and TZ-NP glasses exhibit negligible linear absorption under fs-laser exposure. Although the nonlinear absorption coefficients are also low ($\sim 0.31 \times 10^{-18}$ m^2W^{-1} for TZ glass and 0.28×10^{-18} m^2W^{-1} for TZ-NP glass at 700 nm), intense light-matter interactions arise through nonlinear ionization mechanisms. Specifically, multiphoton ionization dominates in TZ ($\gamma_K = 1.91$), while tunneling ionization prevails in TZ-NP ($\gamma_K = 0.98$), as determined from Keldysh parameter calculations [21]. Full details on the direct laser writing (DLW) configuration are described in Ref. [21].

Laser micromachining was carried out using a range of pulse energies (E_0) and pulses per spot (N = 1–20 000), adjusted via laser repetition rate and scan velocity. For each value of N, sets of 100-μm-long lines, with a 20 μm interline spacing, were fabricated to assess the impact of pulse energy on line width and were used to induce the formation of 3D print patterns inside the glass and to enhance or induce second-harmonic generation. Irradiation parameters are summarized in Tables S1 and S2.

Figure 1 presents fs-laser interaction regimes as a function of pulse number and fluence. Figure 1a,b schematically show the high-N regime (Figure 1a), where energy accumulation induces pronounced thermal and structural modifications, and the low-N regime (Figure 1b), where localized energy deposition restricts changes to narrower and shallower regions.

Optical images (Figure 1c,d) show laser-written lines in TZ and TZ-NP glasses, with increasing dimensions as fluence and N increase. Each serpentine track corresponds to a specific fluence–pulse combination, governed by mechanisms such as multiphoton absorption, tunneling ionization, electron avalanche, and plasma formation [22]. The corresponding height profiles (bottom) confirm that increasing pulse number or fluence deepens and corrugates the channels, reflecting cumulative energy input and potential shockwave involvement [23].

In TZ-NP sample, nanoparticle incorporation alters electron-lattice coupling, modulates the ablation threshold, and reshapes surface morphology. These results demonstrate that microstructuring can be finely tuned through fluence, pulse control, and nanoparticle content, offering tailored designs for integrated photonic or microfluidic platforms.

In addition, DSC analysis (see Figure S1) reveals T_g = 323.6/355.2°C, T_x = 390.5/444.4°C, and T_p = 428.6/467.6°C for TZ/TZ-NP, evidencing increased thermal stability upon nanoparticle incorporation. The stability window $\Delta T = T_x - T_g$ increases from 67.2°C (TZ) to 89.2°C (TZ-NP), while the Hrubý parameter rises from 0.64 to 0.79, both indicating higher resistance to devitrification and a broader processing range. These results, together with density, molar volume, oxygen packing density, refractive index, and band gap (Table S3), confirm the suitability of these glasses for fs-laser microfabrication.

2.2 | Optical Characterization of Fs-Laser-Microfabricated Lines

A fluence-pulse number inscription matrix was generated for TZ and TZ-NP glasses to evaluate their photosensitivity under femtosecond direct laser writing (DLW), with composition-specific fluence thresholds detailed in Tables S1 and S2. Nonlinear optical microscopy images acquired under 850 nm (Figure S2) and 980 nm excitation reveal significant differences in SHG responses between the glasses (Figure 2a,b). For completeness, the optical absorption spectra of both glasses are shown in Figure S3, with the corresponding band gap values of 3.5 eV (TZ) and 3.2 eV (TZ-NP) summarized in Table S3. Figure S4 further presents the morphology of nanoparticles embedded in the TZ-NP glass, including HR-TEM images, SAED pattern, and particle size distribution. The histogram indicates an average

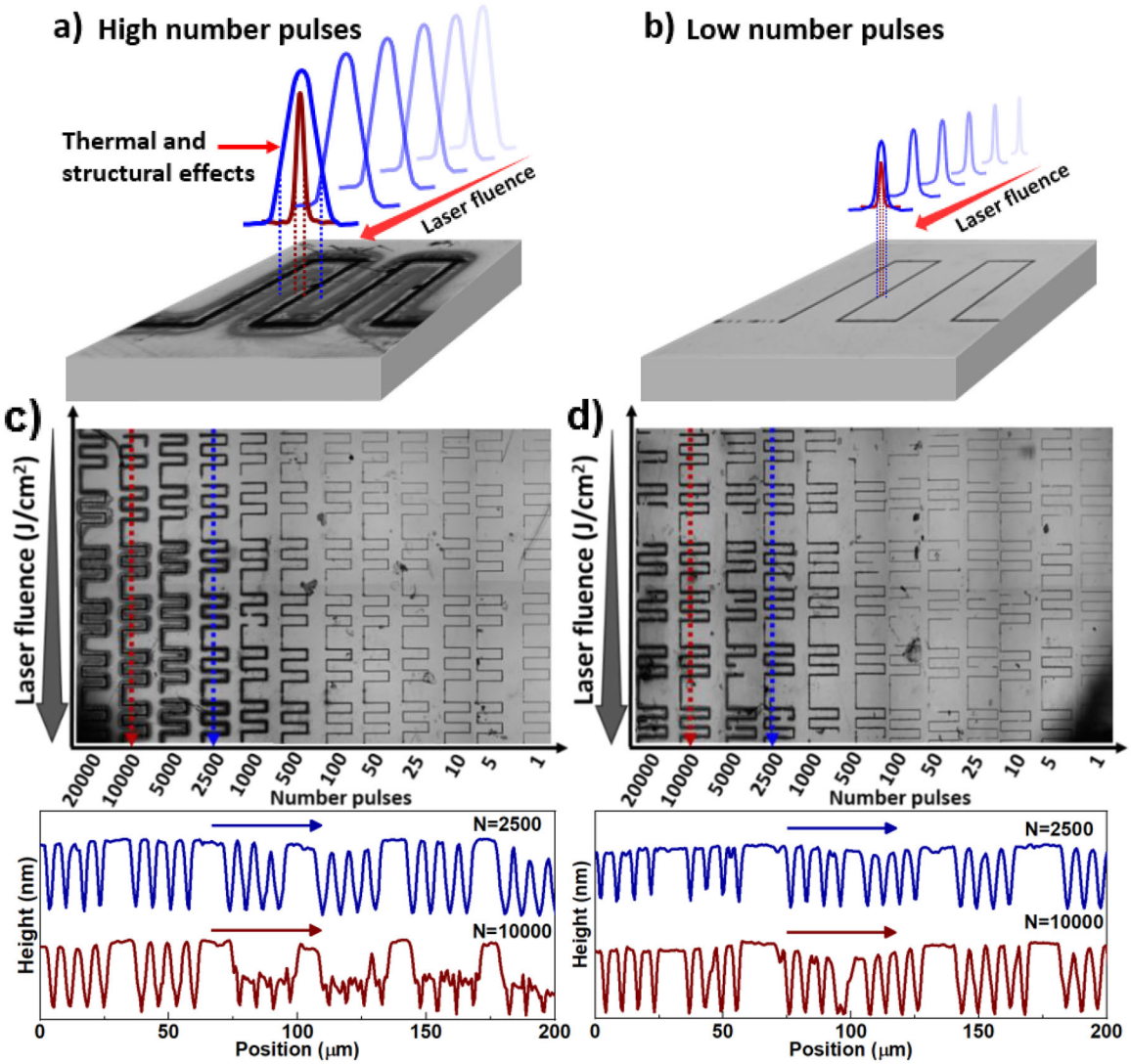

FIGURE 1 | Schematic illustration of fs-laser interaction in tellurite glass for (a) high and (b) low pulse regimes, highlighting cumulative thermal and structural effects. Optical images (top) of fs-laser-processed lines on (c) TZ glass and (d) TZ-NP glass, where the vertical axis indicates laser fluence and the horizontal axis shows the number of pulses (from 1 to 20 000). Each serpentine track corresponds to a distinct combination of fluence and pulse count. The colored dotted rectangles highlight selected lines fabricated with different conditions (e.g., N = 2500 in blue, N = 10 000 in red). The lower plots display surface height profiles taken along these highlighted lines, revealing systematic depth variations that depend on both fluence and pulse count.

diameter of ~30–70 nm and confirms uniform dispersion without significant agglomeration, consistent with the nominal 4 mol% incorporation [20].

SHG intensity profiles vary spatially along the laser-written tracks. Under 850 nm excitation, both glasses exhibit SHG activation above >1000 (Figure S2), indicating a fluence-pulse threshold for nonlinear conversion. Under 980 nm excitation, similar trends emerge, though with enhanced SHG in TZ-NP due to nanoparticle-mediated field effects and rare-earth upconversion pathways (Figure 2a,b).

Normalized SHG intensity trends (Figure 2c) show that, for TZ glass under 850 nm excitation, the SHG increases with fluence up to a maximum (1.9 J/cm^2), then decreases at higher fluences. Similar saturation behavior was observed under 980 nm excitation (Figure 2d), though the intensity increased steadily with fluence before decreasing with lower pulse numbers. In TZ-NP glass, the SHG intensity reached its peak at 3.3 J/cm^2 under 850 nm excitation and at 4.2 J/cm^2 under 980 nm excitation, followed by a significant drop. For both glasses, the intensity decreased progressively at pulse numbers below 500, with TZ-NP glass exhibiting a more pronounced dependency, likely due to thermal accumulation or microstructural effects.

The measured SHG signals and their dependence on the excitation wavelength reflect both the intrinsic nonlinear response of the glass and the modifications induced by the microfabrication process. The emission microscopy images under 980 nm excitation (Figure 2e–g) illustrate the differences between TZ and TZ-NP glasses, specifically in patterned lines processed with 10 000 pulses and a fluence of 3.4 and 4.2 J/cm^2, respectively. In TZ glass, the emission is dominated by a 490 nm SHG

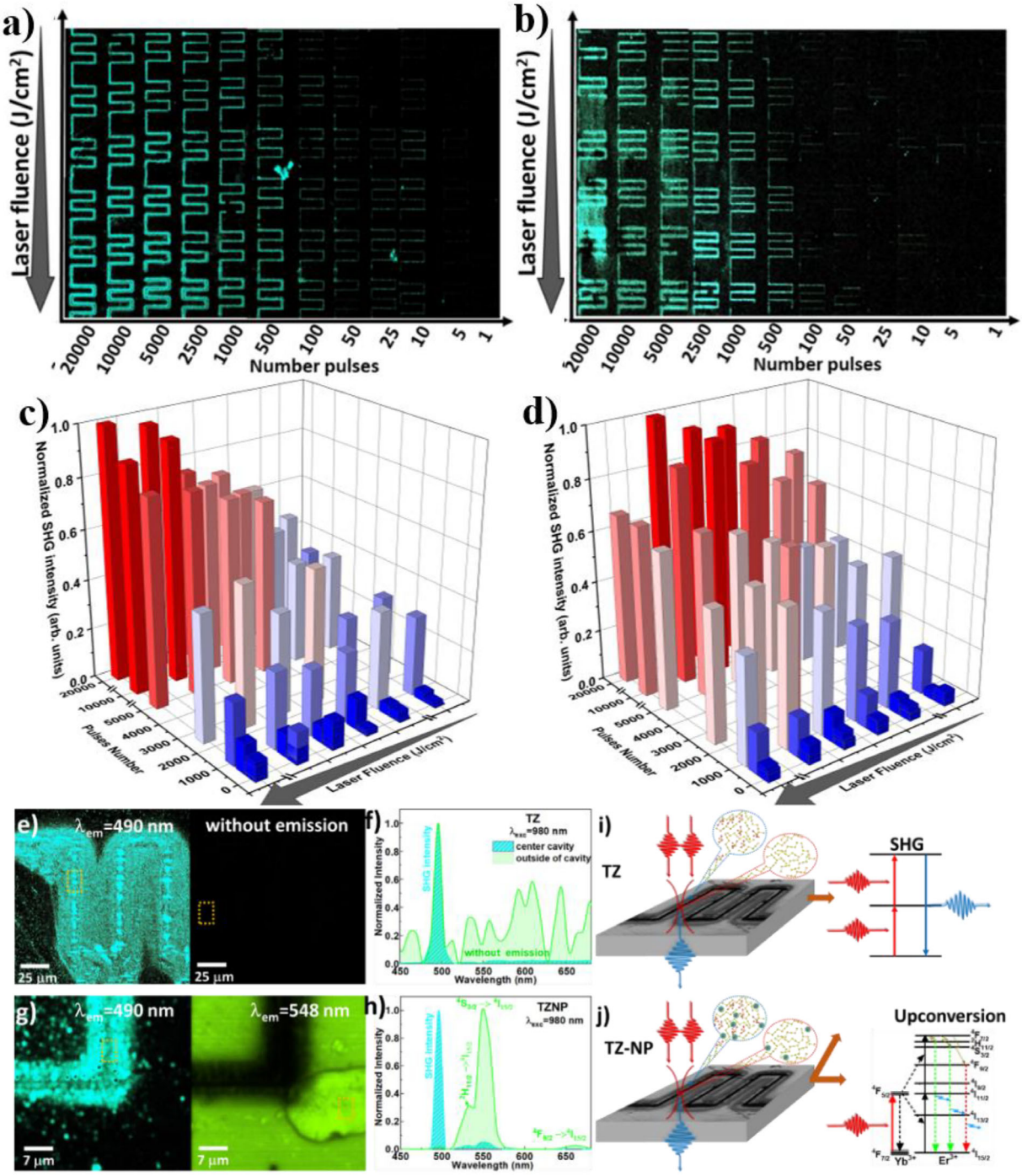

FIGURE 2 | Optical images taken under natural light for (a) TZ and (b) TZ-NP glasses excited at 980 nm with emission 480 nm. Normalized SHG intensity of (c) TZ and (d) TZ-NP glasses excited at 980 nm with emission 480 nm. (e) Emission microscopy images of TZ glass under 980 nm excitation: the left panel shows a non-emitting region, while the right panel displays a bright central cavity SHG at 490 nm. (f) Normalized SHG spectrum of TZ glass, confirming emission at 490 nm. (g) Emission microscopy images of TZ-NP glass under 980 nm excitation: the right panel (548 nm) reveals luminescence from both the central cavity (dashed square) and the surrounding region, and the left panel (490 nm) displays the corresponding SHG intensity. (h) SHG and upconversion spectra of TZ-NP showing Er^{3+} transitions (2H11/2 → 4I15/2 and 4S3/2 → 4I15/2). (i) Schematic of SHG emission (490 nm) mechanism in fs-laser-written TZ glass regions. (j) Combined SHG and Er^{3+}/Yb^{3+} upconversion emission mechanisms in TZ-NP, demonstrating nanoparticle-mediated local field enhancement and energy-transfer pathways.

signal originating from the central cavity, confirming that its nonlinear optical response is primarily due to SHG (Figure 2f). The spectrum collected outside the cavity (green curve) contains no real optical features; the apparent peaks are baseline noise made visible by normalization. Only the cavity center exhibits a distinct 490 nm SHG peak, confirming localization of the nonlinear response within the fs-laser-written region. In contrast, TZ-NP glass exhibits a similar 490 nm SHG response along with strong upconversion luminescence in the green (548 nm) and red (660 nm) regions, attributed to Er^{3+} transitions ($^2H_{11/2}$ →

$^4I_{15/2}$ and $^4S_{3/2} \rightarrow {}^4I_{15/2}$, and $^4F_{9/2} \rightarrow {}^4I_{15/2}$), see Figure 2h. Under 980 nm excitation, Yb^{3+} ions in the $^2F_{5/2}$ state efficiently transfer energy to adjacent Er^{3+} ions, exciting them from $^4I_{15/2}$ to $^4I_{11/2}$. However, since the absorption cross-section of Yb^{3+} at ~980 nm is much larger than that of Er^{3+} ($^4I_{11/2}$), the $Yb^{3+} \rightarrow Er^{3+}$ energy transfer pathway predominates in populating Er^{3+} levels [5]. A second photon absorption or subsequent energy transfer can then promote Er^{3+} to $^4F_{7/2}$, from which it non-radiatively relaxes to $^2H_{11/2}$ or $^4S_{3/2}$. Because of the low phonon energy in the matrix, multi-phonon relaxation is minimized, enabling strong green (548 nm) and red (660 nm) emissions via the $^2H_{11/2}/^4S_{3/2} \rightarrow {}^4I_{15/2}$ and $^4F_{9/2} \rightarrow {}^4I_{15/2}$ transitions, see inset Figure 2h. These emissions, absent in TZ glass, indicate that rare-earth doping and perovskite nanoparticle incorporation enhance radiative and nonlinear optical processes through localized field effects and energy-level modifications. Thus, Figure 2i,j illustrates the distinct emission mechanisms. In TZ glass (Figure 2i), the 490 nm signal arises solely from SHG, likely induced by t-Te nanocrystal, within the laser-written cavity. In contrast, TZ-NP glass (Figure 2j) exhibits both SHG and upconversion emissions, as the Yb^{3+}/Er^{3+} ions are confined in perovskite nanoparticles, which facilitate energy transfer and enhance local fields, resulting in strong green and red emissions. The incorporation of $BaTiO_3$:Er/Yb/Zn nanoparticles is intended to enhance optical functionality rather than modify the laser writing dynamics. Local field amplification from $BaTiO_3$ and $Yb^{3+} \rightarrow Er^{3+}$ upconversion pathways result in stronger SHG and additional UC emissions, as observed in TZ-NP compared to TZ glass (Figure 2i,j).

Beyond these optical effects, the nonlinear optical response correlates with the network's electronic polarizability and optical basicity [24]. According to Dimitrov and Komatsu, the group optical basicities follow the order $\lambda(TeO_4^-) = 1.23 > \lambda(TeO_4^\circ) = 0.99 > \lambda(TeO_3^-) = 0.82$, in agreement with AB initio predictions of polarizability [25]. Distorted TeO_4 units containing non-bridging oxygens (NBOs) exhibit enhanced polarizability, favoring activation of second-order susceptibility (χ^2) in otherwise centrosymmetric matrices [26–28].

Femtosecond laser irradiation disrupts the local centrosymmetry of the tellurite network through nonlinear absorption and transient pressure effects, leading to TeO_4 to TeO_3 conversion, formation of NBOs, local densification, and growth of t-Te nanocrystals [29]. Moreover, asymmetric reorientation of terminal Te—O bonds and the $5s^2$ lone pair on Te(IV) enhance local polarizability, promoting SHG even without long-range order, similar to thermally poled glasses [30]. In TZ-NP glasses, $BaTiO_3$:Er/Yb/Zn nanoparticles further amplify these effects by intensifying local electric fields and modifying electron-lattice interactions. With increasing laser fluence or pulse number, these structural modifications may become more pronounced in both glass types, particularly changes in the $I(TeO_3)/I(TeO_4)$ ratio, NBO accumulation, and the degree of crystallization, thereby impacting the resulting SHG response.

Raman spectroscopy was employed to probe local changes in the glass network to gain deeper insight into this laser-induced structural reorganization. In particular, the Raman band at ~120 cm^{-1} and ~140 cm^{-1}, attributed to t-Te nanocrystals, provides a direct spectral marker for correlating crystallization with nonlinear optical activity.

2.3 | Structural Characterization of Fs-Laser-Microfabricated Regions by XRD and Raman Spectroscopy

Analyzing the structural transformations in fs-laser scanning line patterns through Raman spectroscopy achieved a comprehensive understanding of the origin of the SHG response. This technique was employed to examine how the vibrational properties and coordination of tellurium (Te) atoms evolve across different regions of the samples.

2.3.1 | Structural Evolution before and after Fs-Laser Microfabrication

The essential Raman vibrational modes for TZ and TZ-NP glasses before microfabrication are shown in Figure 3a. The primary modes correspond to the stretching vibrations of TeO_4, TeO_{3+1}, and TeO_3. In TZ glass, the interaction between TeO_4 trigonal bipyramids (tbp) and TeO_3 trigonal pyramids (tp) (or TeO_{3+1}) leads to the formation of bridging oxygen (BO) and non-bridging oxygen (NBO). The addition of Zn as a network modifier drives a transformation of the Te coordination polyhedron from TeO_4 to TeO_3 trigonal pyramid, where a lone pair of electrons occupies one of the sp^3 hybrid orbitals [20]. This modification extends the Te—O interatomic distance, increasing the mobility of the polyhedra and facilitating glass formation [31]. Zn also breaks Te—O—Te linkages in TeO_4 tbp, forming Te═O and Te—O— bonds in TeO_{3+1} and TeO_3 structures, influencing Raman shifts and intensities. In TZ-NP glass, particle incorporation promotes O—M bond breaking and the formation of NBOs, leading to defect sites with low oxygen coordination at NP grain boundaries (Figure 3b).

XRD patterns confirm the non-crystalline nature of both TZ and TZ-NP glasses (Figure 3c). The broader halo in TZ-NP indicates increased structural disorder, likely due to nanoparticle incorporation. This enhanced disorder may promote local field effects favorable for nonlinear optical responses such as SHG. Raman spectra, deconvolution revealed six bands at 422, 487, 621, 666, 730, and 783 cm^{-1} (Figure 3d). The 730 and 783 cm^{-1} bands are attributed to BO (TeO_4 tbp) and NBO (TeO_3 or TeO_{3+1}) structures, while the 666 cm^{-1} band corresponds to asymmetric Te—O—Te vibrations. The band at 487 cm^{-1} represents symmetric Te—O—Te stretching and bending, slightly shifted due to ZnO. For TZ-NP glass, perovskite nanoparticles (NPs) introduce additional spectral features. The Raman spectra can be divided into three key regions: i) bands at 388 cm^{-1} and 497 cm^{-1}, attributed to TeO_4 tbp structures with overlapping contributions from TiO_6 octahedral asymmetry; ii) bands at 571 and 641 cm^{-1}, associated with structural defects and asymmetric Te—O—Te vibrations; and iii) bands at 684 and 781 cm^{-1}, corresponding to symmetric stretching of TeO_4 (BO) and TeO_3/TeO_{3+1} (NBO) structures, respectively [32, 33]. The increased intensity of the 781 cm^{-1} band in TZ-NP glass highlights the role of NPs in breaking Te—O—Te linkages, enhancing dipolar interactions, and increasing nonlinear susceptibility while also reducing optical losses and improving mechanical strength [9].

Alternatively, such changes can be triggered by the interaction of femtosecond laser pulses with transparent materials via multi-photon absorption, leading to localized bond rearrangements and

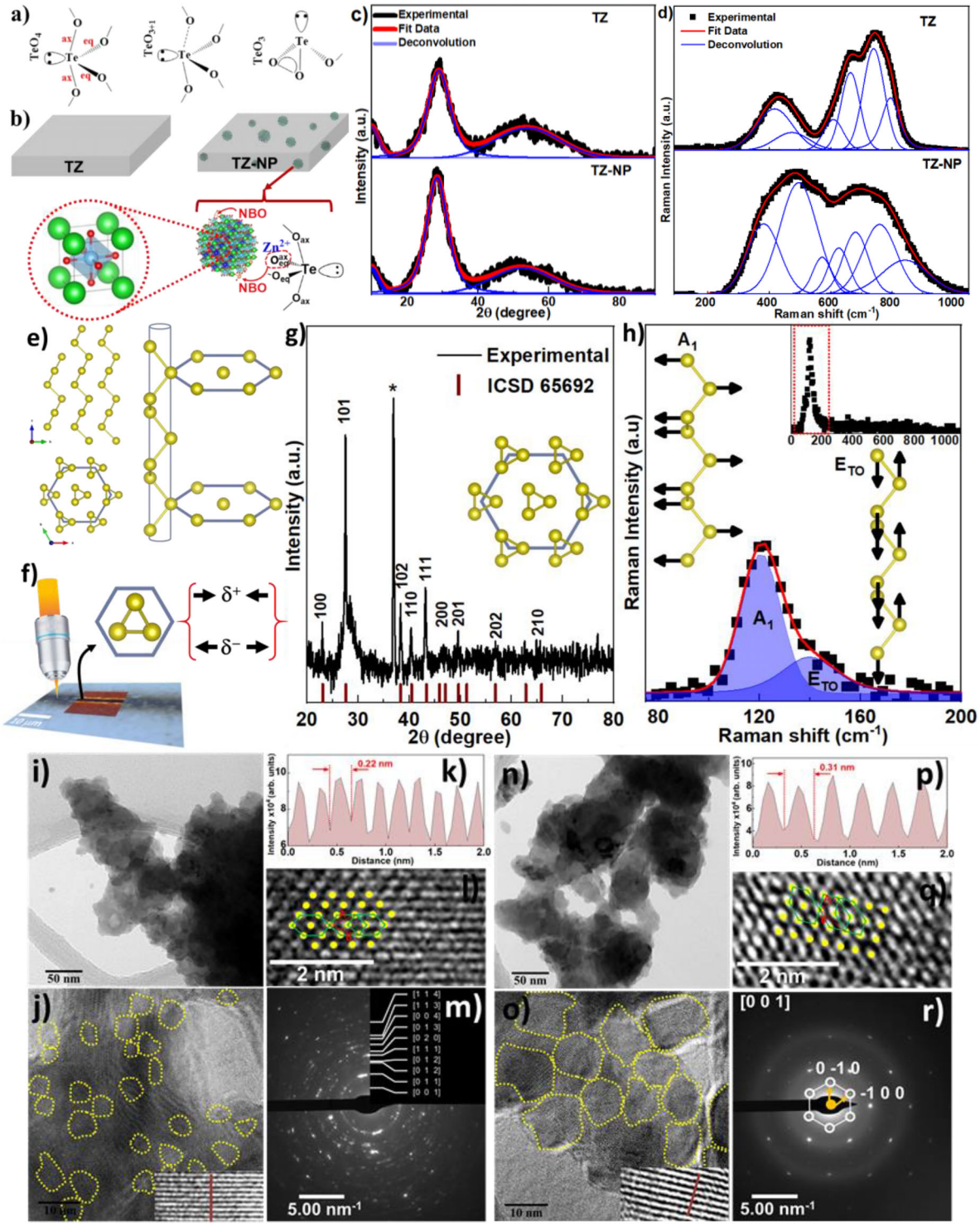

FIGURE 3 | (a) Structural units and rearrangements of TeO_4 and TeO_3 for TZ and TZ-NP. (b) Schematic representation of bond changes in the O atom for TZ and TZ-NP glasses to the formation of NBO. (c) XRD patterns showing the non-crystalline profile of TZ and TZ-NP glasses. (d) Raman spectra of TZ and TZ-NP glasses. (e) Crystal structure of trigonal tellurium (t-Te) with helical chains along the c-axis and hexagonal packing; the right schematic illustrates an isolated helix. (f) Schematic of fs laser irradiation inducing dipole moments under compressive (along [110]) and tensile (along [$\bar{1}\bar{1}$0]) stresses. (g) XRD of t-Te, which corresponds to P3121 hexagonal phase of Te (Inset: Crystal structure of hexagonal Te chains along the c axis). (h) Experimental Raman spectrum highlighting the A1 mode (~120 cm^{-1}) and ETO mode (~140 cm^{-1}), with atomic displacement representations for each vibrational mode (Inset: full Raman spectrum highlighting the amplified low-frequency region). (i–r) HRTEM and SAED analyses of TZ glass after fs-laser irradiation at 100 and 10 000 pulses. (i–m) For 100 pulses: (i) TEM image showing sparse nanocrystals, (j) HRTEM with nanocrystals outlined in yellow, (k) line profile showing interplanar spacing of ~0.22 nm, (l) atomic-resolution HRTEM with overlaid t-Te lattice, (m) SAED pattern displaying diffuse rings, indicating partial crystallinity. (n–r) For 10,000 pulses: (n) TEM image with denser nanocrystals, (o) HRTEM revealing increased nanocrystal size, (p) spacing profile showing ~0.31 nm, (q) atomic-resolution HRTEM matching the t-Te structure, (r) SAED pattern indexed along [001] zone axis, confirming long-range crystalline order of t-Te.

coordination changes [34]. These effects, driven by photoinduced densification or rarefaction, create favorable conditions for the emergence of second-order nonlinear optical responses, such as SHG.

Raman mapping was performed on microfabricated surfaces to analyze these structural changes. Areas irradiated with 10,000 laser pulses at low fluence (0.9 J/cm^2 for TZ and 1.2 J/cm^2 for TZ-NP) and high fluence (3.4 J/cm^2 for TZ and 4.2 J/cm^2 for TZ-NP) were compared. To evaluate structural stability, Raman peak positions will first be analyzed in two distinct spectral regions: a low-frequency region (90–250 cm^{-1}) and a higher-frequency region (250–1000 cm^{-1}). Subsequently, peak intensity variations within these regions will be discussed to elucidate their effects on structural ordering.

The low-frequency region (90–250 cm^{-1}) of the Raman spectrum provides information about the vibrational modes and structural integrity of trigonal tellurium (t-Te) nanocrystals. As illustrated in Figure 3e (left), elemental tellurium crystallizes in a trigonal phase (t-Te) belonging to the chiral space groups $P3_121$ or $P3_221$, characterized by helical chains of Te atoms aligned along the crystallographic c-axis [12, 35]. These chains form a hexagonal array stabilized by van der Waals forces. Their projection onto the *ab* plane reveals sixfold coordination, with three atoms per turn related by screw symmetry operations, giving rise to the crystal's chiral and non-centrosymmetric nature. A complementary view in Figure 3e (right) shows a single helical chain within a cylindrical envelope, highlighting the threefold screw-axis symmetry and intrinsic chirality directly responsible for enabling second-order nonlinear optical processes such as SHG [11, 30, 36].

Upon femtosecond laser irradiation, t-Te nanocrystals nucleate within the tellurite glass matrix. Localized tensile and compressive stresses (Figure 3f–h) distort the lattice, inducing dipole moments along the in-plane directions $[\bar{1}\bar{1}0]$ and [110], effectively breaking centrosymmetry and enabling SHG. Similar fs-laser-induced stress anisotropies have been shown to induce local refractive index changes and symmetry breaking in both glasses and crystals, directly enhancing SHG in $KTiOPO_4$ waveguides [37–39]. Additionally, fs-laser-induced self-organized metallization in tellurite glasses has been linked to stress-driven symmetry alterations [40]. XRD analysis of TZ-NP glass irradiated with 10 000 pulses (Figure 3g) confirms the crystallization into the trigonal t-Te phase (ICSD #65692), while a minor residual peak (marked with an asterisk) suggests unconverted non-crystalline regions. These findings demonstrate that fs-laser irradiation induces local structural rearrangements and enables controlled crystallization of t-Te nanodomains within the glass network.

Complementary vibrational insight was obtained via Raman spectroscopy. According to group theory, the irreducible representation of the optical modes in t-Te is $A_1 + A_2 + 2E$. The Raman-active A_1 mode corresponds to breathing vibration in the ab plane, while the doubly degenerate E modes include $E_{TO}{}^1$ (in-plane rotational motion) and $E_{TO}{}^2$ (asymmetric stretching along the c-axis) [41]. Due to the lack of inversion symmetry, E modes are also IR-active. As shown in Figure 3h, the Raman spectrum reveals a strong A_1 band near 120 cm^{-1} and a weaker $E_{TO}{}^2$ mode around 140 cm^{-1}. Both bands show slight broadening with increasing pulse number or fluence, indicating strain-related variations or phonon confinement [41, 42]. These modes sensitively probe structural symmetry breaking induced by fs-laser irradiation. In parallel, to validate the structural signatures inferred from Raman spectroscopy and directly image the resulting nanostructures, HRTEM and SAED analyses were performed. These analyses confirm the nucleation and growth of t-Te nanocrystals induced by fs-laser irradiation in the TZ glass matrix.

Under irradiation with 100 pulses (Figure 3i–m), ~8 nm nanocrystals appear sparsely distributed (highlighted in yellow in Figure 3j), consistent with an early nucleation regime. HRTEM reveals lattice fringes with an interplanar spacing of ~0.22 nm (Figure 3k), while atomic-resolution imaging (Figure 3l) confirms localized lattice ordering. Simulated structures overlaid on the image match the projected atomic positions of trigonal tellurium, suggesting low-density, short-range ordered domains. In contrast, 10 000 pulses yield increased nanocrystal density and size (~16 nm, Figure 3o), with enhanced structural coherence and clearer lattice fringes (~0.31 nm, Figure 3p). This increase in interplanar distance with pulse number is consistent with local strain relaxation, thermally assisted growth, or a change in the preferred crystallographic orientation of t-Te domains [43, 44]. The atomic-resolution image in Figure 3q confirms the t-Te phase through close agreement between experimental fringes and overlaid atomic models. SAED patterns support this interpretation: under 100 pulses (Figure 3m), diffuse diffraction rings indicate partial crystallinity, while under 10 000 pulses (Figure 3r), they produce sharp diffraction spots along the [001] zone axis, confirming long-range periodicity and alignment with the chiral $P3_121$ structure of trigonal tellurium (ICSD #65692). Reflections from the $(0\bar{1}0)$, $(\bar{1}00)$, and $(\bar{1}\bar{1}0)$ planes correspond to projections within the ab-plane, perpendicular to the Te helical chains (c-axis), reinforcing the assignment of the trigonal t-Te structure. The increase in interplanar spacing, nanocrystal size, and diffraction ordering reveals a progressive transformation driven by cumulative laser exposure, involving stress relaxation, recrystallization, and increased structural ordering. Altogether, these observations substantiate the formation and growth of non-centrosymmetric t-Te nanocrystals as a central mechanism responsible for the enhanced second-harmonic generation observed in laser-processed regions.

The higher-frequency region (250–1000 cm^{-1}) is related to vibrational modes of Te—O bonds in TeO_3 and TeO_4 units. Figure 4a,b and Figure S5a,b present 35 × 35 μm Raman maps of the TeO_3 peak position under different conditions. The color contrast indicates that fs-laser writing modulates TeO_3 modes across irradiated regions. Vertical and horizontal line scans (Figure 4c,d; Figure S5c,d) show shifts in TeO_3 peak positions at different cavity locations (outside, boundary, and center). These shifts become more pronounced with higher fluence, consistent with previous reports on fs-laser-induced glass modifications.

Figure 4e,f and Figure S5e,f provide histograms and additional hyperspectral information on the TeO_3 peak position and FWHM. These large-area maps show distinct average peak positions for TZ and TZ-NP under low and high fluence (see also Figure S6). For TZ glass, the TeO_3 peak shifts from 761.8 cm^{-1} (outside) to 758.1 cm^{-1} (center) under low fluence (Figure 4e), and from 762.3 cm^{-1} (outside) to 773.0 cm^{-1} (center) under high fluence (Figure 4f). In TZ-NP glass, the TeO_3 peak shifts from 759.1 cm^{-1}

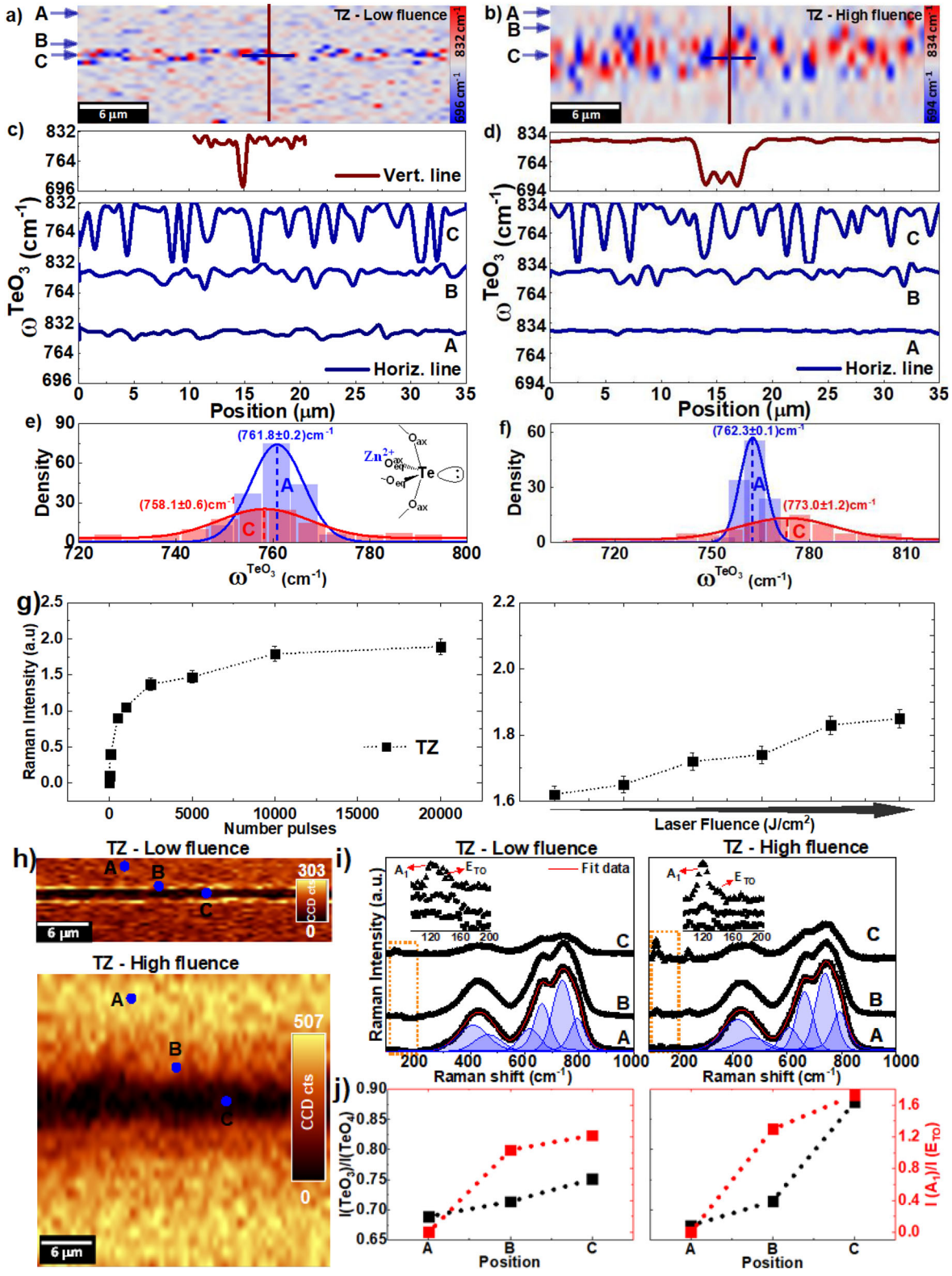

FIGURE 4 | Raman maps of the TeO_3 peak position in TZ glass over a 10 × 35 µm area after fs-laser microfabrication at (a) low and (b) high fluence. (c,d) Corresponding vertical and horizontal profiles showing the TeO_3 band shift at three regions: outside (C), boundary (B), and center (A) of the cavity, under low (c) and high fluence (d). (e, f) Histograms of the TeO_3 peak position for low and high fluence, respectively, with blue and red dashed lines indicating average values. The inset in (e) depicts the local molecular structure in the unmodified region. (g) Raman intensity (obtained from the 120 cm^{-1} peak) as a function of the number of pulses and laser fluence. (h) Raman intensity maps (CCD counts) at low (top) and high fluence (bottom), with marked points A, B, and C corresponding to the regions analyzed. (i) Raman spectra (middle) were measured at each position (A: cavity center; B: boundary; C: outside), with black dots representing the experimental data, red lines indicating the total fits, and blue-shaded peaks showing the deconvoluted vibrational modes. (j) Evolution of both $I(TeO_3)/I(TeO_4)$ and I(A1)/I(ETO) ratios at positions A, B, and C, highlighting structural and vibrational changes across the modified region under different fluences.

(outside) to 756.5 cm^{-1} (center) under low fluence (Figure S5e), and from 757.5 cm^{-1} (outside) to 746.7 cm^{-1} (center) under high fluence (Figure S5f). These results indicate that, while both glasses experience some downshift at low fluence, they diverge at high fluence: TZ shows a 10.7 cm^{-1} upshift at the center cavity, whereas TZ-NP undergoes a further 10.8 cm^{-1} downshift. This difference can be understood in terms of structural reorganization: in TZ-NP, the TeO_3 + NBO → TeO_4 transition is enhanced under high fluence, while in TZ, the formation of additional NBOs may raise ω_{TeO_3}. Although compressive strain affects both glasses due to laser energy transfer, our data suggest that the dominant mechanism behind these shifts lies in the laser-glass interaction modulated by the incorporation of $BaTiO_3$:Er/Yb/Zn nanoparticles in TZ-NP.

Changes in full width at half maximum (FWHM) further clarify these structural transformations. Outside the cavity (low/high fluence), TZ-NP exhibits strong broadening (~82.1 cm^{-1}), whereas TZ displays narrowing (~15.8 cm^{-1}), indicating a reduction in charge doping or defect states due to nanoparticles. Inside the cavity, TZ shows minimal (~3.48 cm^{-1}) broadening, while TZ-NP shows both broadening (~17.0 cm^{-1}) and narrowing (~7.0 cm^{-1}), reflecting a heterogeneous reorganization of tellurite units. These findings suggest that TZ-NP undergoes a reduced TeO_3 structural transformation, with BT nanoparticles stabilizing TeO_4-rich environments.

Following the analysis of peak positions, Raman intensity variations were examined in the same spectral regions to assess changes in structural symmetry and network heterogeneity under different laser fluences and pulse numbers.

In the low-frequency region (90–250 cm^{-1}), significant intensity variations are observed despite stable peak positions (Figure 4g; Figure S5g). These bands, attributed to A_1 and E_{TO} modes of t-Te, consistently increase with pulse number and laser fluence. For TZ glass, the Raman intensity increases by ~150% from 500 to 20 000 pulses and by ~13% with fluence. In contrast, TZ-NP glass exhibits a more rapid enhancement, reaching near-saturation around 5,000 pulses, and achieving an overall enhancement of ~190% across the same pulse range (Figure S5g). Under fixed pulse number (10 000), the Raman intensity initially rises with increasing fluence but declines slightly beyond 108.9 nJ (TZ) and 133.7 nJ (TZ-NP). This behavior suggests a fluence limit above which excessive energy disrupts crystal stability or activates competing mechanisms such as re-amorphization, surface ablation, or thermally driven oxidation that counteract t-Te nanocrystal growth. The enhanced response in TZ-NP highlights the role of $BaTiO_3$:Er/Yb/Zn nanoparticles in amplifying local field effects and thermal accumulation, promoting the formation of crystalline t-Te domains. These results underscore the sensitivity of femtosecond laser-induced crystallization to both energy input and nanoparticle interactions, reinforcing the need for precise control over laser parameters.

In the 250–1000 cm^{-1} spectral range, associated with TeO_3 and TeO_4 vibrational modes, the Raman spectra reveal laser-induced network rearrangements of the glass network. Raman intensity maps of TZ and TZ-NP glasses (Figure 4h; Figure S5h) under varying fluence reveal microfabrication residues and density gradients, which reflect localized symmetry breaking and structural heterogeneity. These spatially dependent features suggest the presence of pressure gradients and stress-driven reorganizations, facilitating TeO_4 → TeO_3 transformations and promoting the formation of t-Te nanocrystals in specific regions. Figure 4i and Figure S5i show spatially resolved spectra across microfabricated regions (A, B, C), indicating partial bond rupture and the coexistence of BO and NBO units. The TeO_3 band intensity at the cavity center (C) is higher in TZ than in TZ-NP, with peak shifts of ~4 cm^{-1} and ~6-9 cm^{-1}, respectively.

As shown in Figure 4j and Figure S5j, the $I(TeO_3)/I(TeO_4)$ ratio increases by ~15% for TZ and ~21% for TZ-NP under high fluence, indicating a stronger network rearrangement in TZ-NP. The spatial evolution of the $I(A_1)/I(E_{TO})$ ratio provides the degree of crystallization of t-Te nanocrystals. In TZ glass, this ratio increases progressively from the periphery (A) to the cavity center (C), reaching ~1.4 under high fluence. In contrast, TZ-NP exhibits a sharper gradient and slightly higher maximum (~1.5), indicating enhanced and more localized crystallization. This behavior reflects the role of nanoparticles in enhancing local electric fields and thermal confinement, favoring anisotropic growth and higher ordering of t-Te nanocrystals. The stronger Raman signals in TZ-NP (Figure S5h) suggest larger crystallite volume or improved coherence, reinforcing nanoparticle-mediated modulation of laser-induced phase transitions.

2.3.2 | Proposed Structural Mechanism for the Formation of T-Te Nanocrystal

Having established the structural characteristics of TZ and TZ-NP glasses from experimental data, we now turn to the structural transformations underlying the non-crystalline-to-crystalline transition. The femtosecond laser-induced formation of trigonal tellurium (t-Te) nanocrystals proceeds via a multistep, nonlinear, and thermally assisted mechanism involving two coupled pathways: i) structural rearrangement of TeO_x units, and ii) reduction-driven crystallization of elemental Te [15, 45]. Raman mapping confirms that both the number of pulses and laser fluence modulate the activation and dominance of these pathways, each influencing the sequence and extent of t-Te nanocrystal formation.

Pulse-number-dependent regime and spatial evolution: Upon femtosecond laser irradiation with increasing pulse numbers (1–20 000), the Raman intensity of t-Te bands (~120 cm^{-1} and 140 cm^{-1}) increases rapidly up to ~5000 pulses, followed by saturation (Figure 4g; Figure S5g). This trend reflects rapid nucleation and subsequent growth saturation of t-Te nanocrystals. In parallel, the $I(TeO_3)/I(TeO_4)$ ratio increases (Figure 4j; Figure S5j), evidencing the depolymerization of the network via TeO_4 → TeO_3 conversion and the formation of NBO sites [9]. These results support two mechanisms:

i) Structural rearrangement of the glass network through:

$$TeO_4 \rightarrow TeO_3 + NBO \quad (1)$$

ii) Redox pathway, involving partial and complete reduction:

$$\text{Electron activation } TeO_3 \rightarrow TeO_3^{2-} + 2e^- \quad (2)$$

Complete reduction

$$TeO_3^{2-} + 2e^- + 6H^+ \rightarrow Te^0_{(s)} + 3H_2O \quad (3)$$

Overall redox reaction:

$$TeO_3^{2-} + 4e^- + 6H^+ \rightarrow Te^0_{(s)} + 3H_2O \quad (4)$$

The reduction process can also be expressed in its most general form:

$$Te^{4+} + 4e^- \rightarrow Te^0_{(s)} \quad (5)$$

This equation expresses the net reduction of Te^{4+} ions, released from TeO_3 or TeO_4 units upon bond cleavage, into crystalline Te^0, driven by the electron-rich plasma generated through multiphoton absorption and avalanche ionization [29, 34, 45]. 2D Raman mappings (Figure S6) reveal that these modifications are spatially heterogeneous, with enhanced t-Te signal and higher $I(TeO_3)/I(TeO_4)$ ratio at the cavity periphery (Figure S7). This anisotropy reflects localized energy accumulation and asymmetric thermal diffusion during scanning, which promote preferential nucleation at the boundary due to favorable thermal gradients and delayed crystallization at the overheated center [46, 47]. Thus, pulse number governs nucleation kinetics and spatial crystallization patterns simultaneously.

The spatial evolution of t-Te nanocrystals under fs-laser writing arises from a dual mechanism involving network depolymerization, redox-driven $Te^{4+} \rightarrow Te^{\circ}$ conversion, and anisotropic growth. At high pulse numbers, cumulative heat accumulation generates radial thermal gradients that assist Te—O bond rearrangements ($TeO_4 \rightarrow TeO_3$/NBO), thereby promoting nucleation and accelerating crystallization and growth of t-Te nanocrystals [48]. This thermo-assisted pathway is consistent with our Raman mapping and established models of heat accumulation in femtosecond laser writing.

Fluence-dependent regime: At a fixed pulse number (10 000), increasing fluence amplifies both the structural rearrangement and redox reduction pathways, but with higher energy density per pulse promoting stronger redox activation [49, 50]. The intensity of the t-Te Raman modes increases with fluence (Figure 4g; Figure S5g), accompanied by a rise in the $I(TeO_3)/I(TeO_4)$ ratio at the cavity core (Figure 4j; Figure S5j), indicating sustained depolymerization and Te^0 formation. In the TZ-NP glass, $BaTiO_3$:Er/Yb/Zn nanoparticles enhance local electric fields and thermal confinement, promoting more efficient TeO_x reduction and anisotropic crystallization, as reflected by a steeper rise in $I(A_1)/I(E_{TO})$, associated with t-Te vibrational modes.

At high fluence, slight attenuation of t-Te signal suggests depletion of reducible TeO_x, reamorphization from overheating, or diminished photon absorption due to surface roughness and scattering by dense nanocrystals [45, 49]. Spatially, crystallization remains peripheral, though steeper temperature gradients shift nucleation dynamics, delayed at the overheated center, enhanced at cooler edges, evidenced by Raman maps (Figure 4h,i; Figure S5h,i). These findings are validated by HRTEM and SAED, which confirm pulse-dependent growth of t-Te nanocrystals (from ~8 nm to ~16 nm), lattice ordering, and long-range periodicity along [001].

Femtosecond laser irradiation induces nonlinear absorption, plasma formation, and ultrafast carrier thermalization, producing sharp temperature gradients across the trace [22, 47, 51]. These gradients can delay nucleation at the overheated center while promoting crystallization at the cooler periphery, consistent with our spatially resolved Raman data. Nucleation likely occurs via both homogeneous (thermally driven fluctuations) and heterogeneous mechanisms, the latter favored by defects, interfaces, or $BaTiO_3$:Er/Yb/Zn nanoparticles. Although bouquet-like or chevron-shaped morphologies were not observed, similar anisotropic growth, guided by directional heat flow and delayed center nucleation, has been reported in fs-laser-crystallized tellurite and lithium niobium silicate glasses [52].

Together, these findings reveal a structure-sensitive mechanism wherein TeO_x depolymerization and laser-triggered redox reactions drive t-Te nanocrystal formation. Spatial dynamics, modulated by temperature gradients, directly influence the nonlinear optical response, as further explored in the SHG analysis.

2.3.3 | Correlation between SHG Intensity and Femtosecond Laser Irradiation

Figure 5 presents the correlation between normalized SHG intensity ($I_{2\omega}$) and the Raman signal at 120 cm^{-1}, attributed to the A_1 mode of triclinic tellurium (t-Te) nanocrystals. This mode is a fingerprint of the formation of non-centrosymmetric domains, whose density increases with pulse number.

Trigonal tellurium crystallizes in the chiral space group $P3_121$ or $P3_221$, enabling electric-dipole-allowed second-order processes. The SHG intensity scales with the density and volume of these domains, as supported by the progressive growth of nanocrystals (from ~8 nm to ~16 nm) observed in HRTEM (Figure 3j,o) and the emergence of sharp [001]-aligned reflections in SAED (Figure 3r), indicating long-range periodicity. Assuming subwavelength dimensions, the SHG intensity is expressed as:

$$I_{2\omega} = \frac{ck^4V^2}{12\pi\epsilon_0}|P(2\omega)|^2 \quad (6)$$

where V is the nanocrystal volume, k the wavevector at 2ω, and $P(2\omega)$ the second-order nonlinear polarization [30, 53, 54]. The enhanced SHG with increasing pulse number is attributed to the enlargement and improved ordering of t-Te nanocrystals.

Since the Raman intensity at 120 cm^{-1} is proportional to crystalline volume, a power-law fit $I_{2\omega} \propto (I_{Raman})^n$ was applied to the data in Figure 5. The fitting yielded $I_{2\omega} = 0.286 \times (I_{Raman})^{2.04}$ for TZ and $I_{2\omega} = 0.284 \times (I_{Raman})^{1.57}$ for TZ-NP. The near-quadratic trend in TZ reflects a volumetric SHG contribution from t-Te, whereas the subquadratic behavior in TZ-NP suggests spatial constraints, likely due to nanoparticle-induced heterogeneous nucleation or local field perturbation. At higher fluences, saturation emerges,

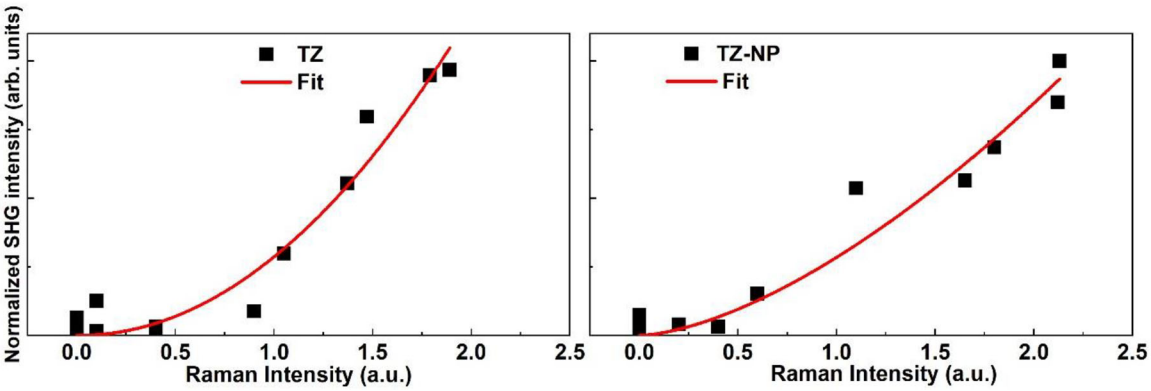

FIGURE 5 | Normalized SHG intensity as a function of Raman intensity at 120 cm^{-1} for TZ (left) and TZ-NP (right) glasses. Black squares: experimental data; red lines: power-law fits.

particularly in TZ-NP, where further increases in Raman intensity no longer yield proportional SHG enhancement. This behavior is consistent with nanocrystal coalescence, thermal relaxation, and structural reorganization that limit additional symmetry breaking.

These results confirm that SHG enhancement originates primarily from the nucleation and growth of chiral, non-centrosymmetric t-Te nanocrystals, driven by structural transformations reflected in the $I(TeO_3)/I(TeO_4)$ ratio. The emergence and evolution of these domains are sensitively probed by the 120 cm^{-1} Raman mode and validated by nanoscale structural evidence from HRTEM and SAED.

2.3.4 | Quantitative Scaling and Efficiency Analysis of SHG

To complement the structural correlation in Section 2.3.3, we performed a quantitative scaling analysis of SHG efficiency to explicitly connect the nonlinear response to the nucleation and growth of t-Te nanocrystals. In the undepleted-pump, non-phase-matched regime, the SHG intensity is given by

$$I_{2\omega} = K(\omega)\, d_{eff}^2 L^2 \sin c^2\left(\frac{\Delta kL}{2}\right) I_{\omega}^2 \tag{7}$$

where $K(\omega) = 2\omega^2/n_{2\omega}n_{\omega}^2c^3\varepsilon_0$, $\Delta k = 2k_{\omega} - k_{2\omega}$, and L the interaction length. This expression corresponds to the standard formulation for SHG in the non-depleted regime [55]. The effective nonlinear coefficient d_{eff} is governed by the density, volume, and acentric ordering of trigonal t-Te nanocrystals, which act as the microscopic sources of SHG.

A log-log plot of $I_{2\omega}$ versus fluence F (constant spot and pulse duration) yields a power-law $I_{2\omega} \propto F^m$ with $m \cong 2$ in the quadratic regime (see Figure 6a). Representative pre-saturation fits at $N = 1000$ under 850 and 980 nm are shown in Figure 6a, from which the slopes m were extracted. At $N \leq 10^3$, TZ shows nearly quadratic slopes ($m = 2$), confirming SHG from volumetric growth and ordering of t-Te nanocrystals, as corroborated by Raman, HRTEM, and SAED. TZ-NP shows comparable values (average $m > 1.5$) but with greater dispersion, reflecting nanoparticle-induced heterogeneous nucleation and local field effects. For $N \geq 2.5 \times 10^3$, both remain crystalline yet exhibit sub-quadratic scaling ($m < 2$), due to heat accumulation, coarsening, and refractive-index changes, which reduce incremental efficiency [48, 56]. Even so, the absolute SHG output increases with crystallinity, and excitation at 980 nm yields stronger 490 nm emission than at 850 nm, despite the larger spread in scaling exponents.

At constant fluence and pulse number, the relative enhancement factor is defined as

$$\varepsilon(F, N, \lambda) = \frac{I_{2\omega}^{(TZ-NP)}}{I_{2\omega}^{(TZ)}} \approx \left(\frac{d_{eff}^{(TZ-NP)}}{d_{eff}^{(TZ)}}\right)^2 .S(\lambda) \tag{8}$$

in which $S(\lambda)$ accounts for small variations in refractive indices and phase mismatch ($S = 1$ under similar conditions). Thus, $d_{eff}^{(TZ-NP)}/d_{eff}^{(TZ)} \approx \sqrt{\varepsilon}$, providing a direct, experiment-based figure of merit for the nonlinear enhancement imparted by nanoparticle incorporation. The evolution of this figure of merit with pulse number at 980 nm is summarized in Figure 6b (values obtained from pre-saturation efficiencies, $\eta = I_{2\omega}/F^2$. This ratio also reflects how $BaTiO_3$:Er/Yb/Zn nanoparticles alter the nucleation and growth pathways of t-Te nanocrystals through local field amplification and modified crystallization kinetics [57].

Finally, the comparison between 850 nm and 980 nm confirms a wavelength dependence consistent with the ω^2 scaling in $K(\omega)$ and variations in phase mismatch. Additional SHG imaging and spectral confirmation for TZ-NP under 850 nm, 900 nm, and 980 nm excitation are presented in Figure S8, providing complementary evidence for the wavelength dependence of the nonlinear response. In TZ-NP, the interplay between t-Te crystallization and rare-earth-induced local field effects modulates SHG efficiency. Although a full polarization-resolved analysis is left for future work, the present scaling laws and efficiency factors demonstrate that the nonlinear response is primarily governed by the crystallization dynamics of t-Te nanocrystals, with secondary modulation from nanoparticle-induced field effects.

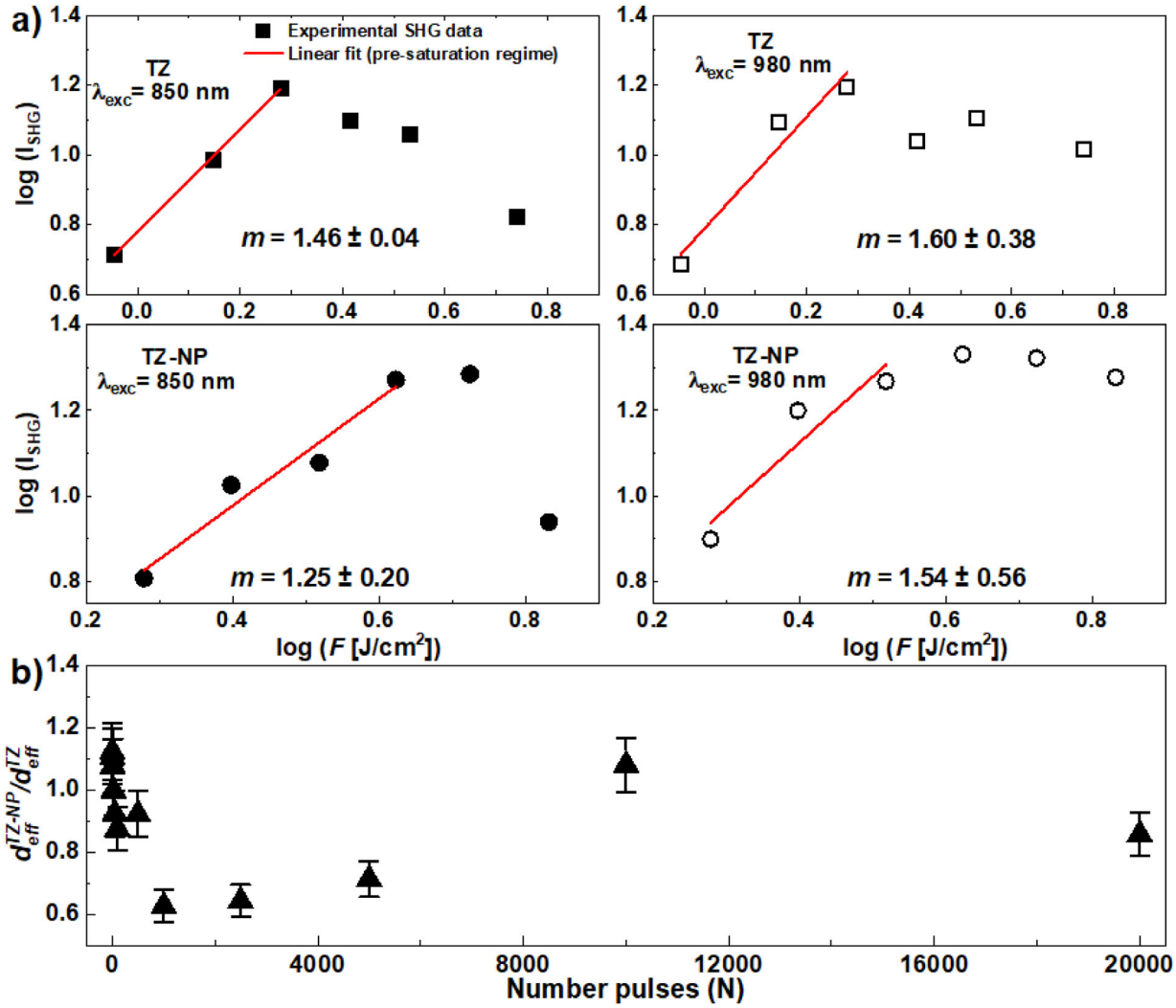

FIGURE 6 | (a) Log-log plot of SHG intensity versus fluence for TZ and TZ-NP glasses at 1000 pulses under 850 nm and 980 nm excitation. Red lines are linear fits in the pre-saturation regime, with slopes (m) indicating the SHG scaling exponent. (b) Nonlinear figure of merit, $d_{eff}^{(TZ-NP)}/d_{eff}^{(TZ)} \approx \sqrt{\varepsilon}$, versus pulse number N at 980 nm. Values obtained from pre-saturation efficiencies. Values were extracted from pre-saturation SHG efficiencies $\eta = I_{2\omega}/F^2$ with $\varepsilon = \eta_{TZ-NP}/\eta_{TZ}$.

3 | Conclusions

Our study demonstrates that fs-laser microfabrication effectively enhances the nonlinear optical properties of tellurite-based (TZ) glasses through structural reorganization and localized crystallization. Pure TZ glass exhibits a maximum SHG intensity of 1.9 J/cm^2 under 850 nm excitation, while TZ-NP glass reaches maxima of 3.3 J/cm^2 (850 nm) and 4.2 J/cm^2 (980 nm), alongside pronounced upconversion luminescence. Raman mapping indicates a clear increase in the I(TeO_3)/I(TeO_4) ratio (15% in TZ and 21% in TZ-NP) in high fluences, correlating directly with enhanced SHG output. The appearance of sharp Raman modes (~120 and 140 cm^{-1}), corroborated by XRD patterns matching the trigonal t-Te phase (ICSD #65692), confirms the fs-laser-induced nucleation of chiral, non-centrosymmetric nanocrystals ($P3_121$). Complementary HRTEM and SAED analyses confirm these observations, revealing increased nanocrystal size (from ~8 nm to ~16 nm) and long-range periodicity along the [001] orientation. Quantitative scaling (m ≈ 2 in TZ, average m > 1.5 in TZ-NP) and $\sqrt{\varepsilon} > 1$ at low-intermediate N confirms nanoparticle-enhanced SHG efficiency despite saturation effects. Altogether, these results highlight a dual mechanism, network depolymerization and redox-driven crystallization, governing the formation of SHG-active t-Te domains. This structure-sensitive, laser-driven pathway offers a robust and tunable platform for integrated nonlinear photonic devices, including on-chip frequency converters and optical modulators.

4 | Experimental Methods

Glasses of chemical composition 70TeO_2-30ZnO (labeled as TZ) and (70TeO_2-30ZnO)-(4.0 mol%)$Ba(Ti_{0.74}Zn_{0.20}Er_{0.03}Yb_{0.03})O_3$ (labeled as TZ-NP) were prepared using the conventional melt-quenching technique. Likewise, the solid-state reaction technique produced perovskite particles $Ba(Ti_{0.74}Zn_{0.20}Er_{0.03}Yb_{0.03})O_3$. For sample preparation, 4 grams of the powders (>99.9% purity) were dried in a platinum crucible and heated at 300°C for 30 min. The mixture was melted in a furnace under oxidizing conditions (oxygen flow of 0.5 L/min)

at 750°C and 850°C for 30 min at each temperature. Afterward, the heated mixture was rapidly poured into a stainless-steel mold preheated at 350°C. After quenching, the solid glass sample was immediately annealed at 350°C for 5 h and then slowly cooled to room temperature. Finally, the samples were polished on both surfaces until (1 mm in thickness) for superior transparency. Thermal stability was evaluated by differential scanning calorimetry (DSC), from which the glass transition (T_g) and crystallization temperatures (T_x) were extracted in Figure S1. Physical and optical parameters, including density, molar volume, oxygen packing density, refractive index, and band gap, are summarized in Table S3.

The fabricated microstructures were characterized by Scanning Electron Microscopy (SEM) using a FEI Inspect-F50 microscope. The crystallinity and phase composition of the irradiated and non-irradiated glass samples were analyzed by X-ray diffraction (XRD) using a Rigaku Ultima IV diffractometer equipped with Cu K_α radiation ($\lambda = 0.15406$ nm), operated at 40 kV and 20 mA. The diffraction patterns were collected over a 2θ range of 20–80°, with a step size of 0.020°. Micro-Raman spectra were recorded with a confocal micro-Raman spectrometer (Witec-ALPHA-300R) equipped with a diode laser operating at a wavelength of 532 nm (output power = 20 mW). The laser was focused on the sample through a 100× objective (NA = 0.9, Olympus) to measure the spectra in backscattering geometry. Data acquisition was performed in the range of 200–2000 cm^{-1}, and the setup was also used to identify phase transformations. HRTEM and SAED analyses were performed using a Talos F200X G2 TEM (Thermo Fisher Scientific) equipped with a high-brightness X-FEG, operated at 200 kV.

The fs-laser micromachining was realized using a diode-pumped Yb:KGW laser system that delivers 216-fs pulses centered at 1030 nm, focused on the TZ and TZ-NP glasses by a 0.65 numerical aperture microscope objective. The microfabrication was studied by varying the repetition rate from 0.1 kHz to 200 kHz, while adjusting the scanning speeds to 12.5 and 25 μm/s, facilitated by precise x-y-z translation stages that positioned the samples. A CCD camera coupled with backlight illumination enabled real-time monitoring of the micromachining process. All experiments were carried out in ambient air, at room temperature, under standard atmospheric conditions. Laser micromachining was conducted with varying pulse energies (E_0) and a range of pulses per spot (N), from 1 up to approximately 20 000. The number of pulses (N) was controlled by adjusting the laser's repetition rate and the scanning speed of the translation stage. For each value of N, sets of 100-μm-long lines, spaced 20 μm apart, were fabricated to assess the impact of pulse energy on line width.

The optical system for SHG microscopy was based on a Zeiss LSM 780 inverted confocal microscope equipped with an EC Plan-Neofluar 10×/0.30 M27 objective. Excitation wavelengths of 850 nm and 980 nm were used, and the resulting micro-luminescence spectra were recorded with the internal photomultiplier tubes (PMTs). Images were acquired at a resolution of 1024 × 1024 pixels, with voxel sizes of 0.83 μm in X and Y, yielding an approximate field of view of 850 × 850 μm. The system was set to record 28 channels in a normal X-Y-Z scan mode, with a single Z-plane and no time-lapse acquisition.

Acknowledgements

Authors are grateful to São Paulo Research Foundation (FAPESP), Grant Nos. 2018/11283-7 and 2021/11484-5; Conselho Nacional de Desenvolvimento Científico e Tecnológico (CNPq), Grant No. 141500/2023-9; Army Research Laboratory (W911NF2110362); and Air Force Office of Scientific Research.

The Article Processing Charge for the publication of this research was funded by the Coordenação de Aperfeiçoamento de Pessoal de Nível Superior - Brasil (CAPES) (ROR identifier: 00x0ma614).

Conflicts of Interest

The authors declare no conflicts of interest.

Data Availability Statement

The data that support the findings of this study are available from the corresponding author upon reasonable request.

References

1. Q. Pan, D. Yang, G. Dong, J. Qiu, and Z. Yang, "Nanocrystal-in-Glass Composite (NGC): A Powerful Pathway From Nanocrystals to Advanced Optical Materials," *Progress in Materials Science* 130 (2022): 100998, https://doi.org/10.1016/j.pmatsci.2022.100998.

2. I. Konidakis, A. Karagiannaki, and E. Stratakis, "Advanced Composite Glasses with Metallic, Perovskite, and Two-Dimensional Nanocrystals for Optoelectronic and Photonic Applications," *Nanoscale* 14 (2022): 2966, https://doi.org/10.1039/D1NR07711B.

3. R. A. H. El-Mallawany, *Tellurite Glasses Handbook: Physical Properties and Data*, (CRC Press, 2019).

4. T. T. Fernandez, M. Sakakura, S. M. Eaton, et al., "Bespoke Photonic Devices Using Ultrafast Laser Driven Ion Migration in Glasses," *Progress in Materials Science* 94 (2018): 68, https://doi.org/10.1016/j.pmatsci.2017.12.002.

5. J. L. Clabel H, G. Lozano C, I. C. Pinto, et al., in Adv. Mater. Res. Technol., ed. S. J. Ikhmayies, (Springer, 2023), 1–52.

6. M. A. Iqbal, J. Qiu, and X. Liu, "Nonlinear Photonics in Glass Systems Doped with Quantum Dots and Plasmonic Nanoparticles," *Nanoscale* 17 (2025): 13094, https://doi.org/10.1039/D5NR00669D.

7. M. Beresna, M. Gecevičius, and P. G. Kazansky, "Ultrafast Laser Direct Writing and Nanostructuring in Transparent Materials," *Advances in Optics and Photonics* 6 (2014): 293, https://doi.org/10.1364/AOP.6.000293.

8. J. Lu, J. Tian, B. Poumellec, et al., "Tailoring Chiral Optical Properties by Femtosecond Laser Direct Writing in Silica," *Light Science & Applications* 12 (2023): 46, https://doi.org/10.1038/s41377-023-01080-y.

9. J. L. Clabel Huamán, K. T. de Paula, F. A. Couto, G. Lozano Calderón, J. D. Vollet-Filho, and C. R. Mendonça, "Enhancing Waveguide Performance in La3+-Doped Tellurite Glasses: Energy-Induced Structural Tuning for Reduced Propagation Loss," *ACS Omega* 10 (2025): 23696, https://doi.org/10.1021/acsomega.5c02610.

10. R. Evans, A. D. Badger, F. Falliès, et al., "Time- and Space-Resolved Optical Probing of Femtosecond-Laser-Driven Shock Waves in Aluminum," *Physical Review Letters* 77 (1996): 3359, https://doi.org/10.1103/PhysRevLett.77.3359.

11. M. Cheng, S. Wu, Z. Z. Zhu, and G. Y. Guo, "Large Second-Harmonic Generation and Linear Electro-Optic Effect in Trigonal Selenium and Tellurium," *Physical Review B* 100 (2019): 035202, https://doi.org/10.1103/PhysRevB.100.035202.

12. A. Londoño-Calderon, D. J. Williams, M. M. Schneider, et al., "Intrinsic helical twist and chirality in ultrathin tellurium nanowires," *Nanoscale* 13 (2021): 9606, https://doi.org/10.1039/D1NR01442K.

13. T. Vasileiadis and S. N. Yannopoulos, "Photo-Induced Oxidation and Amorphization of Trigonal Tellurium: A Means to Engineer Hybrid Nanostructures and Explore Glass Structure Under Spatial Confinement," *Journal of Applied Physics* 116 (2014), https://doi.org/10.1063/1.4894868.

14. S. N. Yannopoulos, "Structure and Photo-Induced Effects in Elemental Chalcogens: A Review on Raman Scattering," *Journal of Materials Science: Materials in Electronics* 31, (2020): 7565, https://doi.org/10.1007/s10854-020-03310-0.

15. G. Torun, A. Romashkina, T. Kishi, and Y. Bellouard, "Femtosecond-Laser Direct-Write Photoconductive Patterns on Tellurite Glass," *Physical Review Applied* 21 (2024), https://doi.org/10.1103/PhysRevApplied.21.014008.

16. M. Li, M. Yan, Y. Pan, et al., "Femtosecond Laser-Induced Glass Refractive Index Change in Tellurite Glass," *Infrared Physics & Technology* 136 (2024): 105028, https://doi.org/10.1016/j.infrared.2023.105028.

17. X. Li, F. Liu, R. Wan, W. Li, and P. Wang, "Femtosecond Laser-Induced Refractive Index Change and Phase-Type Fresnel Zone Plate in Fluorotellurite Glass," *Optics & Laser Technology* 161 (2023): 109216, https://doi.org/10.1016/j.optlastec.2023.109216.

18. A. Butkutė and L. Jonušauskas, "3D Manufacturing of Glass Microstructures Using Femtosecond Laser," *Micromachines* 12 (2021): 499, https://doi.org/10.3390/mi12050499.

19. T. T. Fernandez, S. M. Eaton, G. Jose, R. Osellame, P. Laporta, and J. Solis, "Laser Writing in Tellurite Glasses", in *Technological Advances in Tellurite Glasses*, ed. V. Rivera and D. Manzani, Springer Series in Materials Science, Cham:Springer, 2017, 254, 259–276, https://doi.org/10.1007/978-3-319-53038-3_11.

20. J. L. Clabel H, A. G. Pelosi, J. V. P. Valverde, L. Misoguti, L. De Boni, and C. R. Mendonça, "Structural, Linear and Nonlinear Optical Properties of Perovskite BaTiO3 Tri-Doped Er/Yb/Zn Embedded in Tellurium-Zinc Glass," *Ceramics International* 50 (2024): 5948, https://doi.org/10.1016/j.ceramint.2023.11.085.

21. J. L. Clabel H, K. T. Paula, F. A. Couto, et al., "Optical Waveguides and Work Function Modification in Perovskite Particles Embedded Tellurium-Zinc Glass for Photonic Applications," *Optics & Laser Technology* 186 (2025): 112680, https://doi.org/10.1016/j.optlastec.2025.112680.

22. K. Sugioka and Y. Cheng, "Femtosecond Laser Three-Dimensional Micro- and Nanofabrication," *Applied Physics Reviews* 1 (2014): 041303, https://doi.org/10.1063/1.4904320.

23. A. Heins and C. Guo, "Lasers, Optics, and Optoelectronics," *Journal of Applied Physics* 113 (2013): 223506, https://doi.org/10.1063/1.4810847.

24. V. Dimitrov and T. Komatsu, "Electronic polarizability, optical basicity and non-linear optical properties of oxide glasses," *Journal of Non-Crystalline Solids* 249 (1999): 160, https://doi.org/10.1016/S0022-3093(99)00317-8.

25. T. Komatsu and V. Dimitrov, "Features of electronic polarizability and approach to unique properties in tellurite glasses," *International Journal of Applied Glass Science* 11 (2020): 253, https://doi.org/10.1111/ijag.14776.

26. J. L. Clabel H, J. V. P. Valverde, G. Lozano C, E. Marega, V. R. Mastelaro, and C. R. Mendonça, "Nonlinear optical properties of La3+-Doped tellurite-zinc glasses: Impact of chemical bonding and physical properties via Raman and XPS," *Ceramics International* 51 (2025): 844, https://doi.org/10.1016/j.ceramint.2024.11.069.

27. J. L. Clabel H, G. Lozano, E. Marega, and V. A. G. Rivera, "XPS analysis of bridging and non-bridging oxygen in Yb3+-Er3+-Tm3+-doped zinc-tellurite glasses," *Journal of Non-Crystalline Solids* 553 (2021): 120520, https://doi.org/10.1016/j.jnoncrysol.2020.120520.

28. J. L. Clabel H., G. Lozano C., J. Chacaliaza-Ricaldiet al., "Nonlinear Optical Properties in Pr^{3+}-Er^{3+}-Codoped Tellurite Glasses," *Materials Research Bulletin* 177 (2024): 112832, https://doi.org/10.1016/j.materresbull.2024.112832.

29. G. Torun, T. Kishi, D. Pugliese, D. Milanese, and Y. Bellouard, "Formation mechanism of elemental Te produced in tellurite glass systems by femtosecond laser irradiation," *Advanced Materials* 35 (2023): 2210446, https://doi.org/10.1002/adma.202210446.

30. S. Lee, T. Kishi, and Y. Bellouard, "Wide-Field Polarimetric Second-Harmonic Imaging for Rapid and Nondestructive Investigation of Laser-Induced Crystallization Phenomena," *ACS Nano* 18 (2024): 24929, https://doi.org/10.1021/acsnano.4c05554.

31. N. Effendy, H. A. A. Sidek, M. K. Halimah, and M. H. M. Zaid, "Enhancement on Thermal, Elastic and Optical Properties of New Formulation Tellurite Glasses: Influence of ZnO as a Glass Modifier," *Materials Chemistry and Physics* 273 (2021): 125156, https://doi.org/10.1016/j.matchemphys.2021.125156.

32. J. L. Clabel H, G. Nicolodelli, G. Lozano C, et al., "The Extrinsic Nature of Double Broadband Photoluminescence From the BaTiO 3 Perovskite: Generation of White Light Emitters," *Physical Chemistry Chemical Physics* 23 (2021): 18694, https://doi.org/10.1039/D1CP01765A.

33. T. Uchino and T. Yoko, "Ab Initio Cluster Model Calculations on the Vibrational Frequencies of TeO2 Glass," *Journal of Non-Crystalline Solids* 204 (1996): 243, https://doi.org/10.1016/S0022-3093(96)00423-1.

34. D. Tan, K. N. Sharafudeen, Y. Yue, and J. Qiu, "Femtosecond Laser Induced Phenomena in Transparent Solid Materials: Fundamentals and Applications," *Progress in Materials Science* 76 (2016): 154, https://doi.org/10.1016/j.pmatsci.2015.09.002.

35. G. Qiu, A. Charnas, C. Niu, Y. Wang, W. Wu, and P. D. Ye, "The Resurrection of Tellurium as an Elemental Two-Dimensional Semiconductor," *Npj 2D Materials and Applications* 6 (2022): 17, https://doi.org/10.1038/s41699-022-00293-w.

36. S. Psilodimitrakopoulos, S. Ilin, L. E. Zelenkov, S. Makarov, and E. Stratakis, "Tailoring of the Polarization-Resolved Second Harmonic Generation in Two-Dimensional Semiconductors," *Nanophotonics* 13 (2024): 3181, https://doi.org/10.1515/nanoph-2024-0267.

37. B. McMillen and Y. Bellouard, "On the Anisotropy of Stress-Distribution Induced in Glasses and Crystals by Non-Ablative Femtosecond Laser Exposure," *Optics Express* 23 (2015): 86, https://doi.org/10.1364/OE.23.000086.

38. B. McMillen, C. Athanasiou, and Y. Bellouard, "Femtosecond Laser Direct-Write Waveplates Based on Stress-Induced Birefringence," *Optics Express* 24 (2016): 27239, https://doi.org/10.1364/OE.24.027239.

39. S. L. Li, Y. Song, L. N. Ma, and H. L. Wang, "Femtosecond-Laser-Inscribed Cladding Waveguides in KTiOPO4 Crystal for Second-Harmonic Generation and Y-Branch Splitters," *Frontiers in Physics* 12 (2024): 1341210.

40. G. Torun, T. Kishi, and Y. Bellouard, "Direct-Write Laser-Induced Self-Organization and Metallization Beyond the Focal Volume in Tellurite Glass," *Physical Review Materials* 5 (2021): 055201, https://doi.org/10.1103/PhysRevMaterials.5.055201.

41. D. Spirito, S. Marras, and B. Martín-García, "Lattice Dynamics in Chiral Tellurium by Linear and Circularly Polarized Raman Spectroscopy: Crystal Orientation and Handedness," *Journal of Materials Chemistry C* 12 (2024): 2544, https://doi.org/10.1039/D3TC04333A.

42. Y. Du, G. Qiu, Y. Wang, et al., "One-Dimensional van der Waals Material Tellurium: Raman Spectroscopy Under Strain and Magneto-Transport," *Nano Letters* 17 (2017): 3965, https://doi.org/10.1021/acs.nanolett.7b01717.

43. A. Bhui, S. Roychowdhury, A. Sen, U. V. Waghmare, and K. Biswas, "Free-Standing Few-Layer Tellurene Nanosheets: Simple Solution-Phase Synthesis and Electronic Structure," *Zeitschrift Für Anorganische Und Allgemeine Chemie* 648 (2022): 202200097, https://doi.org/10.1002/zaac.202200097.

44. Y. Dong, B. Zeng, X. Zhang, D. Li, J. He, and M. Long, "Study on the Strain-Induced Mechanical Property Modulations in Monolayer

Tellurene," *Journal of Applied Physics* 125 (2019): 064304, https://doi.org/10.1063/1.5079934.

45. A. A. Manshina, I. I. Tumkin, E. M. Khairullina, et al., "The Second Laser Revolution in Chemistry: Emerging Laser Technologies for Precise Fabrication of Multifunctional Nanomaterials and Nanostructures," *Advanced Functional Materials* 34 (2024): 2405457.

46. J. Xu, Q. Jiang, J. Yang, et al., "A Review on Ultrafast Laser Microwelding of Transparent Materials and Transparent Material–Metals," *Metals (Basel)* 13 (2023): 876, https://doi.org/10.3390/met13050876.

47. M. Macias-Montero, F. Muñoz, B. Sotillo, et al., "Femtosecond Laser Induced Thermophoretic Writing of Waveguides in Silicate Glass," *Scientific Reports* 11 (2021): 8390, https://doi.org/10.1038/s41598-021-87765-z.

48. S. M. Eaton, H. Zhang, P. R. Herman, et al., "Heat Accumulation Effects in Femtosecond Laser-Written Waveguides with Variable Repetition Rate," *Optics Express* 13 (2005): 4708, https://doi.org/10.1364/OPEX.13.004708.

49. R. G. Capelo, J. M. P. Almeida, D. F. Franco, et al., "Controlled Formation of Metallic Tellurium Nanocrystals in Tellurite Glasses Using Femtosecond Direct Laser Writing," *Journal of Materials Research and Technology* 13 (2021): 1296, https://doi.org/10.1016/j.jmrt.2021.05.037.

50. Y. Ito, R. Shinomoto, A. Otsu, K. Nagato, and N. Sugita, "Dynamics of Pressure Waves During Femtosecond Laser Processing of Glass," *Optics Express* 27 (2019): 29158, https://doi.org/10.1364/OE.27.029158.

51. M. V. Shugaev, M. He, Y. Levy, et al., "Laser-Induced Thermal Processes: Heat Transfer, Generation of Stresses, Melting and Solidification, Vaporization, and Phase Explosion," *Handbook Laser Micro-and Nano-Engineering*, (Cham: Springer International Publishing, 2021), 83–163, https://doi.org/10.1007/978-3-030-63647-0.

52. A. Stone, M. Sakakura, Y. Shimotsuma, et al., "Femtosecond Laser-Writing of 3D Crystal Architecture in Glass: Growth Dynamics and Morphological Control," *Materials & Design* 146 (2018): 228, https://doi.org/10.1016/j.matdes.2018.03.016.

53. J. D. Jackson, *Classical Electrodynamics*, (Wiley, 1998), 412.

54. C.-L. Hsieh, Y. Pu, R. Grange, and D. Psaltis, "Second Harmonic Generation From Nanocrystals Under Linearly and Circularly Polarized Excitations," *Optics Express* 18 (2010): 11917, https://doi.org/10.1364/OE.18.011917.

55. R. W. Boyd, in *Nonlinear Optics*, (Elsevier, 2020), 65–134.

56. R. Eaton, S. M. Cerullo, and G. Osellame, in *Femtosecond Laser Micromach*, ed. R. Osellame, R. Cerullo, G. Ramponi, (Springer, 2015), 3–16.

57. D. N. N. V. G. Dmitriev and G. G. Gurzadyan, in *Handbook. Nonlinear Optical Crystals*, ed. A. E. Siegman, (Springer Berlin, 1999), 3–66.

Supporting Information

Additional supporting information can be found online in the Supporting Information section.

Supporting File: lpor70629-sup-0001-SuppMat.pdf.